energies

MDPI

Article

Numerical Investigation on Internal Structures of Ultra-Thin Heat Pipes for PEM Fuel Cells Cooling

Yuqi Han [1], Weilin Zhuge [1,*], Jie Peng [2], Yuping Qian [1] and Yangjun Zhang [1,*]

[1] State Key Laboratory of Automotive Safety and Energy, School of Vehicle and Mobility, Tsinghua University, Beijing 100084, China
[2] AML, Department of Engineering Mechanics, Tsinghua University, Beijing 100084, China
* Correspondence: zhugewl@tsinghua.edu.cn (W.Z.); yjzhang@tsinghua.edu.cn (Y.Z.)

Abstract: Proton exchange membrane fuel cell (PEMFC) powered propulsion has gained increasing attention in urban air mobility applications in recent years. Due to its high power density, ultra-thin heat pipe technology has great potential for cooling PEMFCs, but optimizing the limited internal cavity of the heat pipe remains a significant challenge. In this study, a three-dimensional multiphase model of the heat pipe cooled PEMFC is built to evaluate the impact of three internal structures, layered, spaced, and composite, of ultra-thin heat pipes on system performance. The results show that the heat pipe cooling with the composite structure yields a lower thermal resistance and a larger operating range for the PEMFC system compared to other internal structures because of more rational layout of the internal cavity. In addition, the relationship between land to channel width ratio (LCWR) and local transport property is analyzed and discussed based on composite structural heat pipes. The heat pipe cooled PEMFC with a LCWR of 0.75 has a significant advantage in limiting current density and maximum power density compared to the LCWRs of 1 and 1.33 as a result of more uniform in-plane distributions of temperature and liquid water within its cathode catalyst layer.

Keywords: heat pipe; internal structure; proton exchange membrane fuel cell; thermal management system

Citation: Han, Y.; Zhuge, W.; Peng, J.; Qian, Y.; Zhang, Y. Numerical Investigation on Internal Structures of Ultra-Thin Heat Pipes for PEM Fuel Cells Cooling. *Energies* **2023**, *16*, 1023. https://doi.org/10.3390/en16031023

Academic Editor: Changkook Ryu

Received: 29 November 2022
Revised: 11 January 2023
Accepted: 11 January 2023
Published: 17 January 2023

1. Introduction

Urban air mobility (UAM), an emerging concept of a safe and efficient system for air passengers and cargo transportation operating above populated areas, has drawn considerable interest as a means of resolving the conflict between the need for efficient mobility and congested ground transportation in high-density cities [1–3]. Numerous companies have worked on developing enabling components for UAM, and the majority of their prototypes are electric vertical takeoff and landing (eVTOL) vehicles [1,4,5]. Propulsion system is the core component of the eVTOLs, where lithium-ion batteries are commonly employed. However, eVTOLs serverd by power batteries are limited in range and endurance [2]. Due to high specific energy, zero emission and low operating temperature, proton exchange membrane fuel cells (PEMFC) are regarded as an effective technological approach to considerably increase the payload and range of eVTOLs [6–8]. Comparing to batteries, PEMFCs are compelling candidates for powering eVTOLs with mission over 50 miles, and show tremendous technoeconomic advantages at a range of 60 miles [2,3].

Fuel cell systems for UAM applications are mainly constrained by low power density [7,9]. PEMFC systems with power greater than 5kW typically employ liquid-cooled thermal management subsystems, which have the drawbacks of complex structure, high power consumption, and large volume and weight [10,11]. Improving the efficiency of the thermal management subsystem and reducing its size and weight is one of the research hotspots in improving the power density of PEMFC systems [12]. Owing to the benefits of small size, lightweight, high effective thermal conductivity, excellent temperature uniformity, and no pumping power consumption, heat pipe cooling in PEMFC has recently drawn increasing attention [13–16].

Faghri first proposed embedding the evaporators of conventional columnar heat pipes into graphite bipolar plates for fuel cell cooling, leading to the original heat pipe cooled fuel cell solution [17]. According to the representative feasibility experiment results of conventional columnar heat pipe cooling, the maximum temperature difference of the heat pipe evaporator is less than 2 °C, and its maximum temperature is less than 90 °C under a heat flux of 1.8 W cm^{-2} [18]. Although feasible for fuel cell cooling, conventional columnar heat pipes are replaced by flat heat pipes for better surface temperature uniformity and power density [19]. Researchers have evaluated the performance of the flat heat pipe cooled fuel cells using various cooling strategies. Huang et al. tested a flat heat pipe cooled PEMFC stack with heat pipes designed to transport heat along the width direction. The temperature gradient within a single cell was less than 1 °C under all inclination angles [20]. Wang et al. tested a PEMFC stack cooled by heat pipes that transported heat in a length-wise direction. When compared to the traditional PEMFC, the average temperature and maximum temperature difference of heat pipe cooled PEMFC are reduced by 11.58 °C and 5.10 °C, respectively; the mass power density and volume power density could be improved by 12.2% and 9.5%, respectively [21]. Zhao et al. investigated a cooling strategy with one flat heat pipe for every two cells. According to the experimental results, roughly half of the heat generated by the stack could be removed through heat pipes by increasing the cooling air flow rate [22]. Research into several types of flat heat pipe cooling has shown remarkable results in terms of temperature uniformity and power density enhancement. However, few researchers have focused on the internal structure of the flat heat pipe when employing heat pipe cooling for PEMFC, which plays a significant role in heat pipe cooling performance.

Wick structures are crucial components of heat pipes. Development of high capillary performance wicks is the primary approach to enhancing the thermal performance of thin heat pipes. Numerous studies have attempted to improve the capillary properties of wicks through structure optimization and surface treatments [23,24]. Tang et al. tested 1.0 mm thick ultra-thin flat heat pipes with various mesh numbers, and results showed that a higher mesh wick number can lower heat resistance while increasing working fluid flow resistance [25]. Zhou et al. fabricated and investigated 1.0 mm thick heat pipes with biporous spiral woven mesh wicks. The thermal performance and capillary rate-of-rise experiments were conducted, and the results indicated that the maximum heat transfer capacity of the heat pipe with biporous wick is higher than that with monoporous wick [26]. Furthermore, scholars have proposed and researched a variety of composite wick types that offer both superior permeability and capillarity [27,28].

For ultra-thin heat pipes, optimization of the limited internal cavity in the heat pipe is a more low-cost and effective way to improve the thermal performance. In contrast to the layered structure used in thick flat heat pipes, setting vapor cores on both sides of the wick (i.e., spaced structure, see Figure 1) is commonly applied under extremely low thickness conditions. Huang et al. performed a parametric analysis to compare the flow resistance of two types of heat pipe internal structures, layered and separated, and the results revealed that the maximum heat transfer capability of spaced structure was much higher than that of layered structure when the internal cavity thickness was less than 0.3 mm, while minimal difference between the two was observed when the internal cavity thickness was greater than 0.6 mm [29]. Zhou et al. examined the impact of the liquid-to-vapor passage area ratio on the thermal performance of ultra-thin heat pipe experimentally [30]. The highest maximum heat transfer capability was obtained by heat pipes with 4 mm wide wicks, which was 4.25 times greater than that with 2 and 7 mm wide wicks. Although heat pipes with spaced structures have sufficient thickness for the vapor core to reduce the vapor flow resistance and improve maximum heat transfer capability, the lack of phase change heat transfer at the contact surface between the vapor core and the heated shell may lead to hot spots. As shown in Figure 1, the composite structure could combine the advantage of the spaced structure and the layered structure. Huang et al. fabricated and tested multiple ultra-thin heat pipes with the composite internal structures, and the results showed higher maximum heat transfer capability and thermal conductivity compared to

the previous ultra-thin heat pipes with the layered structures [31,32]. Although different heat pipe internal cavity arrangements have been developed, current research has generally focused on a specific type of heat pipe internal structure, and performance comparison and optimization of different internal structures remains a challenge.

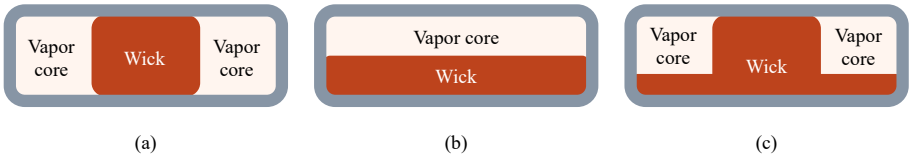

Figure 1. Cross-section of flat heat pipes with different internal structures: (**a**) Spaced structure. (**b**) Layered structure. (**c**) Composite structure.

Overall, thinner flat heat pipes are preferred for high power density systems, and optimizing the limited internal cavity in heat pipes is an effective approach to increasing the thermal performance of the ultra-thin heat pipe cooled PEMFCs. Several academics have conducted preliminary studies on flat heat pipes for PEMFC cooling, but comprehensive exploration into the effects of the internal structure of the flat heat pipe on system power density is still lacking. The dependence between the internal structure of the heat pipes and the internal transport phenomenon of the PEMFCs has remained unclear. Accordingly, it is essential to examine and compare the system performance of heat pipe cooled PEMFC with different internal structures of heat pipes.

In this study, the performance of three internal structures (spaced, layered, and composite) of heat pipes has been systematically investigated and compared based on heat pipe bipolar plate (HPBP) cooled PEMFCs. A three-dimensional multiphase non-isothermal single channel model of the HPBP cooled PEMFC is developed. And how land to channel width ratio (LCWR) affect the temperature distribution and local transport phenomena of the HPBP cooled PEMFC is also profoundly investigated. It is hoped that this study could be used to guide the design of high power density heat pipe cooled PEMFCs.

2. Numerical Model

2.1. Physical Problem

The different heat pipe internal structures in this study are designed based on HPBP cooling, as it is a promising solution for high power density thermal management. In HPBP cooled PEMFCs, the sealed bipolar plates serve as the heat pipe shell, which could significantly shorten the heat transfer pathway from the membrane electrode assembly (MEA) to the wick-vapor core interfaces compared to conventional heat pipe cooled PEMFCs. Figure 2 shows the following heat pipe internal structure designs: layered, modified layered, spaced with large vapor core, spaced with small vapor core, modified spaced, and composite. The cell thickness of layered and modified layered sturcture is a bit thinner than the others. Due to the large wick thickness, the conventional layered structure outperforms the modified layered structure in terms of total thermal resistance. The conventional spaced structure with various vapor core sizes both have the problem of providing too few gas-liquid interfaces, which is not favorable to phase change. Eliminating these three unreasonable structures, the remaining three structures, (a) layered, (e) modified spaced, and (f) composite, are adopted for the subsequent modeling and comparison analysis.

As demonstrated in Figure 3, the domains of the three-dimensional models of the HPBP cooled PEMFC consist of a PEMFC and two half-heat pipes, including cathode/anode bipolar plate (CBP/ABP), cathode/anode gas channel (CGC/AGC), cathode/anode gas diffusion layer (CGDL/AGDL), cathode/anode catalyst layers (CCL/ACL), polymer exchange membrane (MEM), wicks and vapor cores. The working fluid within heat pipes absorbs heat and vaporizes at the fuel cell-mounted evaporators. Then it flows to the condensers, and the condensed fluid will be delivered back to the evaporators under capillary action.

The fuel cell has an active area of 50×1.4 mm^2, and the gas channel cross-section area is 0.7×0.4 mm^2. The thicknesses of gas diffusion layers, ACL, CCL, and MEM are 0.2 mm,

0.003 mm, 0.01 mm, and 0.018 mm, respectively. The LCWR is set to 1 in the internal structural effect analysis for heat pipes. All the heat pipes designed in this paper are less than 2 mm thick, belonging to the ultra-thin heat pipe. The thickness of wick and bipolar plate sheet of the half-heat pipe are both 0.1 mm. Water is employed as the working fluid of heat pipes, and its thermophysical properties are obtained at 80 °C. Other associated model parameters and operation conditions are summarized in Table 1.

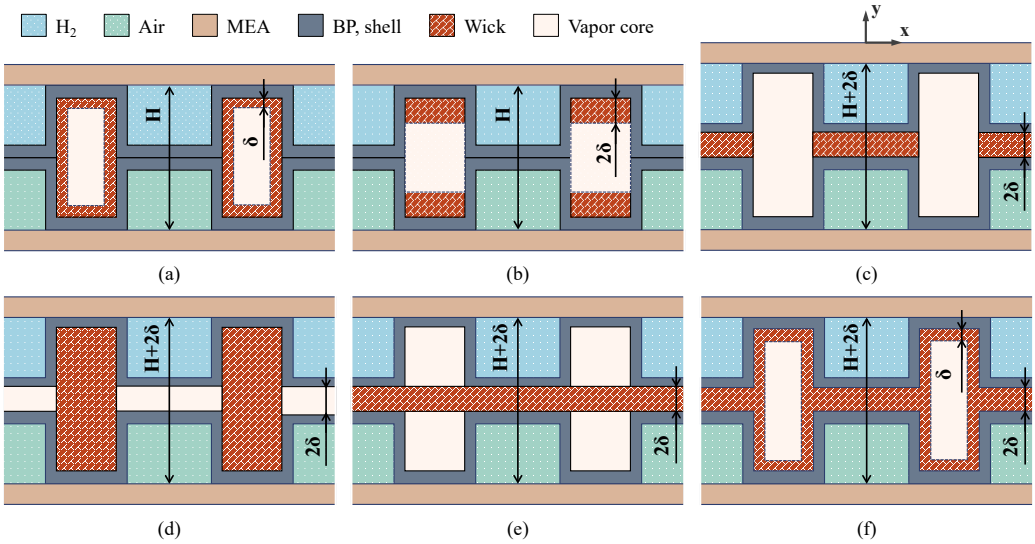

Figure 2. Schematics of the HPBPs with different internal structures: (**a**) Layered structure. (**b**) Modified layered structure. (**c**) Spaced structure with large vapor core. (**d**) Spaced structure with small vapor core. (**e**) Modified spaced structure. (**f**) Composite structure.

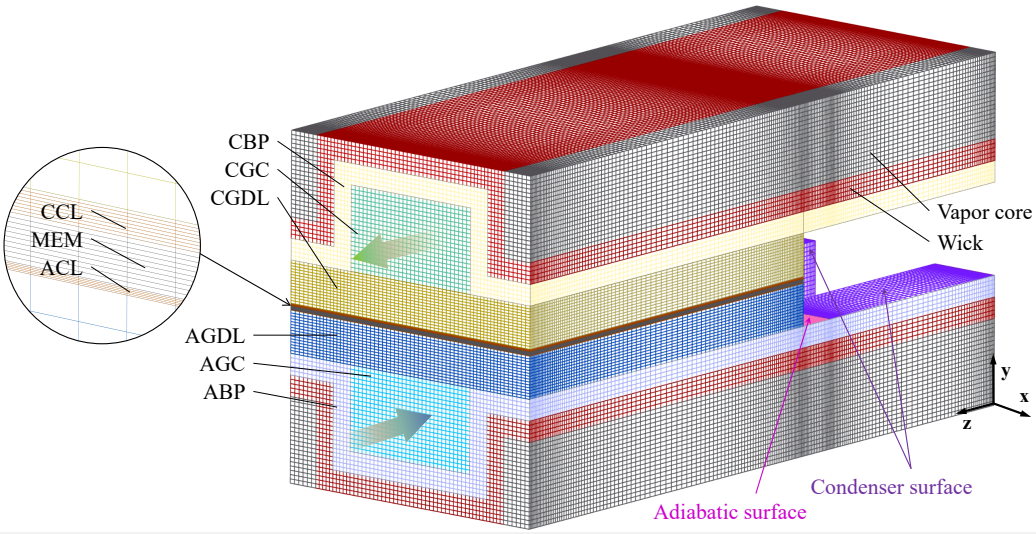

CBP/ABP: cathode/anode bipolar plate; CGC/AGC: cathode/anode gas channel; CGDL/AGDL: cathode/anode gas diffusion layer; CCL/ACL: cathode/anode catalyst layer; MEM: polymer exchange membrane.

Figure 3. Cross-section of flat heat pipes with different internal structures.

Table 1. Model parameters and operation conditions.

Parameter	Value	Unit
Operating pressure	1.5	atm
Cell temperature	353.15	K
Relative humidity	anode: 95%; cathode: 95%	
Stoichiometric ratio	anode: 2; cathode: 2	
Electric conductivity (BPs. GDLs, CLs) [33]	20000, 8000, 5000	S m^{-1}
Porosity of GDLs [34]	0.6	
Contact angle (GDLs, CLs) [35]	120°, 100°	
Intrinsic permeability (GDLs, CLs) [36]	2.0×10^{-12}, 1.0×10^{-13}	m^2
Thermal conductivity of GDLs [35]	in-plane: 21; through-plane: 1.7	W m^{-1} K^{-1}
Thermal conductivity (BPs, CLs, MEM) [35]	16.27, 1, 0.95	W m^{-1} K^{-1}
Equivalent weight of ionomer [33]	1.1	kg mol^{-1}
Density of ionomer [33]	1980	kg m^{-3}
Condensation and evaporation rates of liquid water [36]	100	s^{-1}
Adsorption and desorption rates of dissolved water [36]	1.3	s^{-1}
Latent heat [37]	2.308×10^6	J kg^{-1}
Entropy change [38]	163.28	J mol^{-1} K^{-1}
Reference concentration [34]	hydrogen: 56.4; oxygen: 3.39	mol m^{-3}
Henry's coefficient of hydrogen [33]	4560	Pa m^3 mol^{-1}
Henry's coefficient of oxygen [33]	$0.11552 \exp\left(14.1 + 0.0302\lambda - \frac{666}{T}\right)$	Pa m^3 mol^{-1}
Transfer coefficient [14]	anode: 1; cathode: 1	
Porosity of wicks	0.71	
Permeability of wicks	2.1×10^{-11}	m^2
Thermal conductivity of wicks	1.16	W m^{-1} K^{-1}
Mesh number of wicks	300	in^{-1}
thickness of wicks	0.1	mm
capillary radius of wicks	0.042	mm
contact angle of wicks	0°	

2.2. Assumptions and Governing Equations

The HPBP cooled PEMFC model is developed based on the following assumptions:

1. The HPBP cooled fuel cell is assumed to operate in steady-state;
2. The gas mixture property is calculated using the ideal gas law;
3. The flow in the PEMFC and the heat pipe is incompressible and laminar.
4. Homogeneous mist flow in the gas channels of the PEMFC;
5. Gravitational effect is neglected;
6. The thermal and electrical contact resistances between different layers are ignored;
7. Phase change in heat pipe occurs only at the wick-vapor core interfaces.

The conservation equations governing mass, momentum, species, liquid water, dissolved water, energy, and charge are obtained and listed below.

Mass conservation:

$$\nabla \cdot (\rho \boldsymbol{u}) = S_{\mathrm{m}} \tag{1}$$

where, S_{m} denotes the total mass source, which incorporates changes in gas phase mass caused by the consumption/production of gas species. The consumption/production of gas species is mainly related to the phase transition and electrochemical consumption inside the fuel cell.

Momentum conservation:

$$\nabla \cdot \left(\frac{\rho \boldsymbol{u}\boldsymbol{u}}{\varepsilon^2 (1-s)^2} \right) = -\nabla P + \mu \nabla \cdot \left(\nabla \left(\frac{\boldsymbol{u}}{\varepsilon (1-s)} \right) + \nabla \left(\frac{\boldsymbol{u}^T}{\varepsilon (1-s)} \right) \right) - \frac{2}{3} \mu \nabla \left(\nabla \cdot \left(\frac{\boldsymbol{u}}{\varepsilon (1-s)} \right) \right) + S_{\boldsymbol{u}} \tag{2}$$

where, ε and s refer to the porosity and liquid water saturation of the porous media.

Species conservation:

$$\nabla \cdot (\rho \boldsymbol{u} Y_{\mathrm{i}} - \rho D_{\mathrm{i,eff}} \nabla Y_i) = S_{\mathrm{i}} \tag{3}$$

where, i represents hydrogen, oxygen, vapor, and nitrogen. Y_{i} and $D_{\mathrm{i,eff}}$ denote mass fraction and effective diffusivity of the gas species i, respectively.

Energy conservation:

$$\left(\rho c_{\mathrm{p}}\right)_{\mathrm{eff}} \nabla \cdot (\boldsymbol{u} T) = \nabla \cdot (k_{\mathrm{eff}} \nabla T) + S_T \tag{4}$$

where, $\left(\rho c_{\mathrm{p}}\right)_{\mathrm{eff}}$ is defined as the effective volumetric heat capacities of fluid and solid, k_{eff} denotes the effective thermal conductivity.

Liquid water:

$$\nabla \cdot \left(\frac{K_{\mathrm{l,eff}}}{\mu_{\mathrm{l}}} \frac{dP_{\mathrm{cap}}}{ds} \rho_{\mathrm{l}} \nabla s \right) = S_{\mathrm{l}} \tag{5}$$

where, $K_{\mathrm{l,eff}}$ and μ_{l} represent the effective permeability and viscosity of the liquid water. P_{cap} is the capillary pressure.

Dissolved water:

$$\frac{\rho_{\mathrm{MEM}}}{\mathrm{EW}} \nabla \cdot (-D_{\lambda,\mathrm{eff}} \nabla \lambda) = S_\lambda \tag{6}$$

where, λ reflects the membrane water content, ρ_{MEM} denotes the density of ionomer, EW is the equivalent weight of ionomer. $D_{\lambda,\mathrm{eff}}$ is the effective diffusivity of the dissolved water.

Electronic charge conservation:

$$\nabla \cdot (-\kappa_{\mathrm{e,eff}} \nabla \phi_{\mathrm{e}}) = S_{\phi_{\mathrm{e}}} \tag{7}$$

Protonic charge conservation:

$$\nabla \cdot (-\kappa_{\omega,\mathrm{eff}} \nabla \phi_\omega) = S_{\phi_\omega} \tag{8}$$

where, ϕ_{e} and ϕ_ω refer to the potentials of electrons in solid phase and protons in the ionomer phase, respectively. $\kappa_{\mathrm{e,eff}}$ and $\kappa_{\omega,\mathrm{eff}}$ are the effective electronic and protonic conductivity.

The electrochemical reaction rates can be calculated using the Butler-Volmer equation, the anode Butler-Volmer equation is shown as below:

$$j_{\mathrm{a}} = i_{0,\mathrm{a}}^{\mathrm{ref}} i_{\mathrm{T,a}} A_{\mathrm{eff}} \left(\frac{P_{\mathrm{H_2}}}{H_{\mathrm{H_2}} C_{\mathrm{H_2}}^{\mathrm{ref}}} \right)^{0.5} \left(\exp\left(\frac{\alpha_a F \eta_{\mathrm{act,a}}}{RT} \right) - \exp\left(-\frac{\alpha_c F \eta_{\mathrm{act,a}}}{RT} \right) \right) \tag{9}$$

In order to take into account difficulty of oxygen transport and structural details of the CCL, the cathode Butler-Volmer equation is modified based on spherical agglomerate model:

$$j_{\mathrm{c}} = 4F \frac{P_{\mathrm{O_2}}}{H_{\mathrm{O_2}}} \left(\frac{1}{E_{\mathrm{r}} k_{\mathrm{c}} (1 - \varepsilon_{\mathrm{CL}})} + \frac{r_{\mathrm{agg}} + \delta_\omega + \delta_{\mathrm{l}}}{r_{\mathrm{agg}}} \left(\frac{\delta_\omega}{A_{\mathrm{agg},\omega} D_{\mathrm{O_2},\omega}} + \frac{\delta_{\mathrm{l}}}{A_{\mathrm{agg,l}} D_{\mathrm{O_2,l}}} \right) \right)^{-1} \tag{10}$$

where, j, H, E_{r}, k_{c}, α, η_{act}, i_0^{ref}, i_{T}, A_{eff}, $A_{\mathrm{agg},\omega}$, and $A_{\mathrm{agg,l}}$ denote volumetric current density, Henry's coefficient, effectiveness factor, reaction rate constant, transfer coefficient, activation overpotential, reference exchange current density, the dependence of i_0^{ref} on temperature, the effective reaction surface area, the ionomer effective agglomerate surface area, and liquid water effective agglomerate surface area, respectively.

The activation overpotential in ACL and CCL could be given by the following expressions:

$$\eta_{\mathrm{act,a}} = \phi_{\mathrm{e}} - \phi_\omega \tag{11}$$

$$\eta_{\mathrm{act,c}} = \phi_{\mathrm{e}} - \phi_\omega - V_{\mathrm{oc}} \tag{12}$$

The open circuit voltage (V_{oc}) can be expressed based on the Nernst's equation:

$$V_{oc} = 1.23 - 8.5 \times 10^{-4}(T - 298.15) + 4.31 \times 10^{-5} T\left(\ln\left(\frac{P_{H_2}}{101325}\right) + \frac{1}{2}\ln\left(\frac{P_{O_2}}{101325}\right)\right) \quad (13)$$

The transport properties and the source terms in the governing equations are given in Tables 2 and 3.

Table 2. Transport properties.

Parameter	Expression	Unit
Water saturation pressure [33]	$\log_{10}\left(\frac{P_{sat,l}}{101325}\right) = -2.1794 + 0.02953(T - 273.15) - 9.1837 \times 10^{-5}(T - 273.15)^2 + 1.4454 \times 10^{-7}(T - 273.15)^3$	Pa
Effective gas diffusivity [36]	$D_{i,eff} = (\varepsilon(1-s))^{1.5} D_i$	$m^2\ s^{-1}$
Dissolved water diffusivity [33]	$D_{\lambda,eff} = \begin{cases} 3.1 \times 10^{-7}\lambda(\exp(0.28\lambda) - 1.0)\exp\left(\frac{-2346.0}{T}\right) & 0 < \lambda \le 3 \\ 4.17 \times 10^{-8}\lambda(161.0\exp(-\lambda) + 1.0)\exp\left(\frac{-2346.0}{T}\right) & 3 < \lambda \le 17 \\ 4.1 \times 10^{-10}\left(\frac{\lambda}{25.0}\right)^{0.15}\left(1.0 + \tanh\left(\frac{\lambda - 2.5}{1.4}\right)\right) & \lambda > 17 \end{cases}$	$m^2\ s^{-1}$
Effective gas phase permeability [39]	$K_{g,eff} = (1-s)^n K, \quad n = \begin{cases} 3 & \text{CLs} \\ 4.5 & \text{GDLs} \end{cases}$	m^2
Effective liquid phase permeability [39]	$K_{l,eff} = s^n K, \quad n = \begin{cases} 3 & \text{CLs} \\ 4.5 & \text{GDLs} \end{cases}$	m^2
Electro-osmotic drag coefficient [39]	$n_d = \frac{2.5\lambda}{22}$	
Equilibrium water content [33]	$\lambda_{eq} = \begin{cases} 0.043 + 17.81a - 39.85a^2 + 36.0a^3 & 0 \le a \le 1 \\ 14.0 + 14.0(a - 1.0) & 1 < a \le 3 \end{cases}$	
Water activity [39]	$a = \frac{P_v}{P_{sat,l}}$	
Effective electronic conductivity [39]	$\kappa_{e,eff} = \begin{cases} \kappa_e & \text{BPs} \\ (1-\varepsilon)^{1.5}\kappa_e & \text{GDLs} \\ (1-\varepsilon-\omega)^{1.5}\kappa_e & \text{CLs} \end{cases}$	$S\ m^{-1}$
Effective protonic conductivity [33]	$\kappa_{\omega,eff} = \begin{cases} \kappa_\omega & \text{MEM} \\ (1-\varepsilon_{CL})\left(1 + \frac{(\omega_{agg}-1)}{(1+\delta_\omega/r_{agg}+\chi)^3}\right)\kappa_\omega & \text{CLs} \end{cases}$	$S\ m^{-1}$
Protonic conductivity [33]	$\kappa_\omega = (0.5139\lambda - 0.326)\exp\left(1268\left(\frac{1}{303.15} - \frac{1}{T}\right)\right)$	$S\ m^{-1}$
Phase change between vapor and liquid water [36]	$S^{v\leftrightarrow l} = \begin{cases} \zeta_{cond}\varepsilon(1-s)\frac{P_v - P_{sat,l}}{RT} & P_v \ge P_{sat,l} \\ \zeta_{evap}\varepsilon s\frac{P_v - P_{sat,l}}{RT} & P_v < P_{sat,l} \end{cases}$	$mol\ m^{-3}\ s^{-1}$
Phase change between dissolved water and liquid water [39]	$S^{\lambda\leftrightarrow v} = \begin{cases} \gamma_a\frac{\rho_{MEM}}{EW}(\lambda_{eq} - \lambda) & \text{ACL} \\ \gamma_d\frac{\rho_{MEM}}{EW}(\lambda_{eq} - \lambda) & \text{CCL} \end{cases}$	$mol\ m^{-3}\ s^{-1}$

Table 3. Source terms of conservation equations for the PEMFC.

Source Term		Unit
$S_m = \begin{cases} -\left(S^{v\leftrightarrow l} + S^{\lambda\leftrightarrow v}\right)M_{H_2O} - \frac{j_a}{2F}M_{H_2} & \text{ACL} \\ -\left(S^{v\leftrightarrow l} + S^{\lambda\leftrightarrow v}\right)M_{H_2O} - \frac{j_c}{4F}M_{O_2} & \text{CCL} \\ -S^{v\leftrightarrow l}M_{H_2O} & \text{GDLs} \end{cases}$		$kg\ m^{-3}\ s^{-1}$
$S_u = -\frac{\mu_g}{K_{g,eff}}u_g$	CLs and GDLs	$kg\ m^{-2}\ s^{-2}$
$S_T = \begin{cases} \kappa_{e,eff}\lvert\nabla\phi_e\rvert^2 & \text{BPs} \\ \kappa_{e,eff}\lvert\nabla\phi_e\rvert^2 + LS^{v\leftrightarrow l}M_{H_2O} & \text{GDLs} \\ \kappa_{e,eff}\lvert\nabla\phi_e\rvert^2 + \kappa_{\omega,eff}\lvert\nabla\phi_\omega\rvert^2 + L\left(S^{v\leftrightarrow l} + S^{\lambda\leftrightarrow v}\right)M_{H_2O} + \lvert j_a\eta_a\rvert & \text{ACL} \\ \kappa_{e,eff}\lvert\nabla\phi_e\rvert^2 + \kappa_{\omega,eff}\lvert\nabla\phi_\omega\rvert^2 + L\left(S^{v\leftrightarrow l} + S^{\lambda\leftrightarrow v}\right)M_{H_2O} + \lvert j_c\eta_c\rvert + \left\lvert\frac{j_cT\Delta S}{2F}\right\rvert & \text{CCL} \\ \kappa_{\omega,eff}\lvert\nabla\phi_\omega\rvert^2 & \text{MEM} \end{cases}$		$W\ m^{-3}$

Table 3. *Cont.*

Source Term	Unit
$S_{H_2} = -j_a \frac{M_{H_2}}{2F}$ ACL	kg m^{-3} s^{-1}
$S_{O_2} = -j_c \frac{M_{O_2}}{4F}$ CCL	kg m^{-3} s^{-1}
$S_{H_2O} = \begin{cases} -\left(S^{v\leftrightarrow l} + S^{\lambda\leftrightarrow v}\right) M_{H_2O} & \text{CLs} \\ -S^{v\leftrightarrow l} M_{H_2O} & \text{GDLs} \end{cases}$	kg m^{-3} s^{-1}
$S_l = S^{v\leftrightarrow l} M_{H_2O}$ CLs and GDLs	kg m^{-3} s^{-1}
$S_\lambda = \begin{cases} \nabla \cdot \left(\frac{n_d}{F}\left(\kappa_{\omega,\text{eff}} \nabla \phi_\omega\right)\right) & \text{MEM} \\ \nabla \cdot \left(\frac{n_d}{F}\left(\kappa_{\omega,\text{eff}} \nabla \phi_\omega\right)\right) + S^{\lambda\leftrightarrow v} & \text{ACL} \\ \nabla \cdot \left(\frac{n_d}{F}\left(\kappa_{\omega,\text{eff}} \nabla \phi_\omega\right)\right) + S^{\lambda\leftrightarrow v} + \frac{j_c}{2F} & \text{CCL} \end{cases}$	mol m^{-3} s^{-1}
$S_{\phi_e} = \begin{cases} -j_a & \text{ACL} \\ j_c & \text{CCL} \end{cases}$	A m^{-3}
$S_{\phi_\omega} = \begin{cases} j_a & \text{ACL} \\ -j_c & \text{CCL} \end{cases}$	A m^{-3}

2.3. Maximum Heat Transfer Capability

The fact that the internal structure of the heat pipe determines its maximum heat transfer capacity is one of the crucial differences between heat pipe cooling and conventional cooling. Generally, capillary limit is the determining limitation for ultra-thin heat pipes. When the capillary pressure is insufficient to pump the liquid back to the evaporator, the capillary limit is reached. Then the evaporator will dry out, and heat transfer from the evaporator to the condenser will break down.

Therefore, ultra-thin heat pipes should be operated to ensure that the maximum capillary pumping pressure, $\Delta P_{cap,max}$, exceeds the total pressure drop whithin heat pipes, including the liquid pressure drop, ΔP_l, and the vapor pressure drop, ΔP_v.

$$\Delta P_{cap,max} \geq \Delta P_l + \Delta P_v \tag{14}$$

The maximum capillary pressure developed within the heat pipe wick structure is given by the Laplace-Young equation [40]. In Equation (15), σ represents the surface tension of working fluid, θ denotes the contact angle, and r_{eff} refers to the capillary radius. In this study, a superhydrophilic mesh screen with a mesh number of 300 in^{-1} and a thickness of 0.1 mm (δ, see Figure 2) is employed. The capillary radius, contact angle, and maximum capillary pressure of the heat pipes are calculated to be 0.042 mm, 0° (full wetting), and 2984.4 Pa, respectively.

$$\Delta P_{cap,max} = \frac{2\sigma \cos\theta}{r_{eff}} \tag{15}$$

2.4. Boundary Conditions

As demonstrated in Figure 3, symmetric conditions are imposed at the two ends in the x direction, and periodic conditions are defined at the two ends in the y direction. The reactant flow direction in the CGC is opposite to that in the CGC. The mass flow inlet boundaries and pressure outlet boundaries are imposed at the inlets and outlets of the GCs, respectively. As to the potentials of electrons, Dirichlet boundary conditions, $\phi_{e,a} = 0$ and $\phi_{e,c} = V_{cell}$, are applied to the end surfaces of the ABP and CBP in the PEMFC, respectively.

$$\dot{m}_{\mathrm{in,a}} = \frac{\rho_{\mathrm{a}} \xi_{\mathrm{a}} i A_{\mathrm{act}}}{2FC_{\mathrm{H_2}}} \tag{16}$$

$$\dot{m}_{\mathrm{in,c}} = \frac{\rho_{\mathrm{c}} \xi_{\mathrm{c}} i A_{\mathrm{act}}}{4FC_{\mathrm{O_2}}} \tag{17}$$

$$C_{\mathrm{H_2}} = \frac{P_{\mathrm{in,a}} - RH_{\mathrm{a}} P_{\mathrm{sat}}}{RT} \tag{18}$$

$$C_{\mathrm{O_2}} = \frac{0.21(P_{\mathrm{in,c}} - RH_{\mathrm{c}} P_{\mathrm{sat}})}{RT} \tag{19}$$

where, $\dot{m}_{\mathrm{in,a}}$ and $\dot{m}_{\mathrm{in,c}}$ refer to the mass flow rates at anode and cathode inlets, ξ, i, A_{act}, and V_{cell} stand for the stoichiometry ratio, the average current density, active area, and cell voltage, respectively.

It was assumed that the temperature at the wick-vapor core interfaces was saturated, which is determined by the Clausius-Clapeyron equation. The phase change velocities at the wick-vapor core interfaces are assumed normal to the interface, which is obtained by the energy balance there. Consequently, the boundary conditions at the wick-vapor core interfaces could be given as,

$$\dot{m}_{\mathrm{pc}} = \rho_{\mathrm{v}} u_{\mathrm{v}} A_{\mathrm{pc}} = \rho_{\mathrm{l}} u_{\mathrm{l}} A_{\mathrm{pc}} \tag{20}$$

$$-k_{\mathrm{eff}} A_{\mathrm{pc}} \frac{\partial T}{\partial n} + \dot{m}_{\mathrm{pc}} c_{\mathrm{p,l}} T_{\mathrm{l}} = -k_{\mathrm{v}} A_{\mathrm{pc}} \frac{\partial T}{\partial n} + \dot{m}_{\mathrm{pc}} c_{\mathrm{p,v}} T_{\mathrm{v}} + \dot{m}_{\mathrm{pc}} L \tag{21}$$

$$T_{\mathrm{v}} = T_{\mathrm{l}} = T_{\mathrm{sat}} = \left(\frac{1}{T_{\mathrm{ref}}} - \frac{R}{ML} \ln \frac{P_{\mathrm{v}}}{P_{\mathrm{ref}}} \right)^{-1} \tag{22}$$

where, m_{pc}, u_{v}, u_{l}, T_{v}, T_{l}, P_{v}, P_{ref}, and T_{ref} represent the mass flow rate of phase change, the vapor velocity at the wick-vapor core interfaces, the liquid velocity at the interfaces, the interface temperature at vapor core side, the interface temperature at wick side, the interface pressure at vapor core side, reference pressure, and reference temperature.

At the condenser surfaces of the heat pipe, uniform negative heat flux is implemented. Additionally, the vapor temperature at the middle position of the adiabatic section is 80 °C. This enables for the comparison of the performance of heat pipes with varied internal structures under the same boundary conditions, which also corresponds to the outlet condition widely employed for fuel cell liquid cooling.

2.5. Numerical Procedures and Model Validation

The commercial computational fluid dynamics (CFD) software, ANSYS FLUENT 17.0, is utilized to solve the conservation equations. The correlations for transport parameters and source terms are numerically imposed by user-defined functions (UDF). For the pressure-velocity coupling, the SIMPLE algorithm is used, and the algebraic multigrid (AMG) approach is employed to speed up computation. Each variable is subjected to a convergence criterion with a residual below 10^{-6}. A grid-independent analysis is conducted to avoid grid-size effect. Six grid numbers, 207,306, 468,448, 902,200, 1,175,960, 1,589,192, and 1,805,900, are tested, and the predicted current density and total pressure drop variations are less than 1.5% when the grid number is more than 902,200. The grid number of 902,200 is chosen for conducting the numerical analysis.

In order to validate the PEMFC model, the polarization curve obtained from a published experimental study [34] of PEMFC is used for comparison. As illustrated in Figure 4, the simulated curve shows good agreement with the experimental data. The developed heat pipe model is validated by comparing the published numerical results of the temperature distribution within a layered structural heat pipe [41]. The temperature difference over the wick-vapor core interface, the total temperature difference between the evaporator and the condenser, and the temperature difference within the evaporator are included in

comparsion. Figure 5 shows that the numerical results of the heat pipe are reasonably agreeable. Therefore, the model utilized in this study is reliable for analyzing the impact of the internal structure of the heat pipe on system performance.

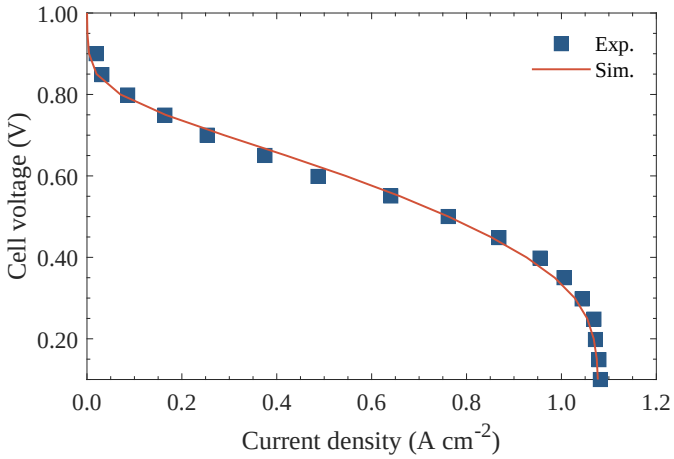

Figure 4. Comparison with steady-state measured data of the PEMFC [34].

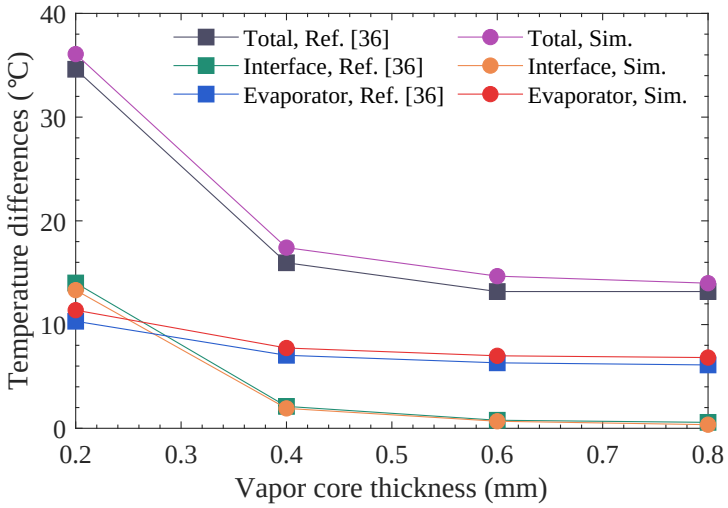

Figure 5. Comparison with numerical results of the ultra-thin heat pipe [41].

3. Results

This section is divided into two parts. In the first part, the influence of the internal structure of the heat pipe on the thermal performance of the HPBP cooled PEMFC system is systematically investigated, and the optimal internal structure of the heat pipe obtained is used for the second part of the study. Since the heat pipe dimensions in HPBP are closely coupled with the mass transfer resistance in PEMFC, optimizing the HPBP dimensions such as gas channel height, gas channel width, and land width is of more significance for system performance improvement compared to the traditional heat pipe cooled PEMFC. To achieve the highest system power density, further research is conducted in the second part on the impact of the dimensionless parameter, land to channel width ratio, on the local transport properties of the HPBP cooled PEMFC.

3.1. Effect of the Internal Structure of the Heat Pipe on Thermal and Electrochemical Performance

Maximum heat transfer capability, maximum temperature, and temperature uniformity over the middle plane of the CCL are the primary criteria used for assessing the performance of heat pipe cooling. In this study, the temperature uniformity is determined

by the maximum temperature difference and the index of uniform temperature (IUT). The IUT is defined as follows:

$$IUT = \frac{\int |T - \overline{T}| dA}{\int dA} \tag{23}$$

$$\overline{T} = \frac{\int T dA}{\int dA} \tag{24}$$

where $\overline{T}$ and A denote the average surface temperature and surface area, respectively.

The total internal pressure drop of the heat pipe must be smaller than the maximum capillary pressure in order to successfully transport the required heat load. As shown in Figure 6, at current densities of about 2.09 A cm^{-2}, 3.49 A cm^{-2}, and 3.41 A cm^{-2}, respectively, the total internal pressure loss corresponding to the three internal structures of the HPBPs—layered, modified spaced, and composite—exceed the maximum capillary pressure. This implies that the operating range of the fuel cell cooled by the layered structural HPBP is about 40% less than that cooled by other HPBPs. The detailed data of the total pressure loss inside the HPBPs at a cell voltage of 0.45 V are listed in Table 4. The smaller cross-sectional area of the wick in layered structural HPBP (see Figure 2), which results in a substantially high internal liquid pressure drop, is the main contributor to its poor maximum heat transfer capability. The total internal pressure drops of HPBPs with the modified spaced and composite structures are comparable, whereas the composite structure corresponds to a smaller liquid pressure drop. It should be noted that the HPBP with the modified spaced structure has the lowest vapor pressure drop, despite the fact that its vapor core is divided into two segments in the height direction; the difference in vapor pressure drops between composite and layered structures is remarkable, even though they share similar dimensions. This revealed that the vapor pressure drop within ultra-thin heat pipes is primarily governed by the smallest shape dimensions. Even though a high pressure loss appears owing to the smallest shape dimensions, increasing other cross-sectional dimensions will still assist in reducing the vapor pressure drop.

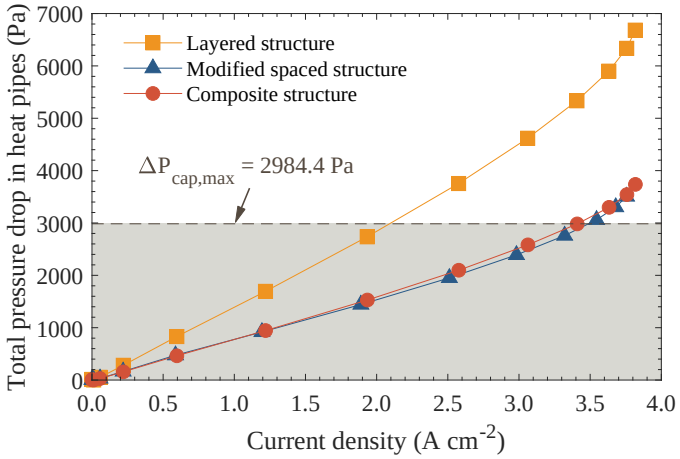

Figure 6. Comparison of the maximum heat transfer capability of the HPBPs with different internal structures.

Table 4. Pressure drops in HPBPs with different internal structures at a cell voltage of 0.45 V.

Parameters	Layered Structure	Modified Spaced Structure	Composite Structure
ΔP_v (Pa)	1805.7	510.4	1224.8
ΔP_l (Pa)	3528.2	2249.0	1757.5
ΔP_{total} (Pa)	5333.9	2759.4	2982.3

When PEMFCs operate at temperatures above 90 °C, membrane drying typically occurs, raising issues with ionic resistance, ohmic loss, and material degradation [10,42]. The maximum temperatures of PEMFCs cooled by HPBPs with different internal structures are illustrated in Figure 7. The increment in the maximum temperature increases with increasing current density for all HPBP cooled PEMFCs. PEMFC cooled by modified spaced structural HPBP has the highest maximum temperature when compared to composite and layered structural HPBP, and the disadvantage becomes more notable with greater current density. Due to operating temperature limitations, the PEMFC with the modified spaced structural HPBP cooling can only operate at less than 2.44 A cm^{-2}, while the PEMFCs cooled with the composite and layered structural HPBPs can both operate at less than 3.50 A cm^{-2}. The primary reasons for this are that the modified spaced structural HPBP has longer heat transfer pathway and higher thermal resistance.

The maximum temperatures are generally located at CCL due to the presence of a considerable overpotential. Figure 8a,b show the maximum temperature difference and the IUT over the middle plane of the CCL, respectively. As shown in the figures, the temperature uniformity decreases when increasing the current density of HPBP cooled PEMFCs. The composite and layered structure significantly outperforms the modified spaced structure in terms of temperature uniformity in the high current density region. When comparing Figures 7 and 8, it can be seen that the fuel cell operating range is significantly less constrained by temperature uniformity than by maximum temperature.

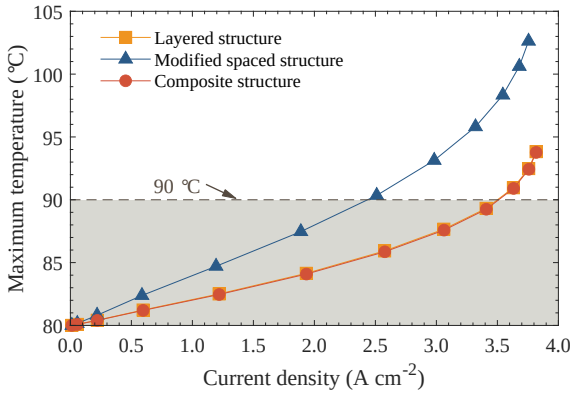

Figure 7. Comparison of the maximum temperatures of PEMFCs cooled by HPBPs with different internal structures.

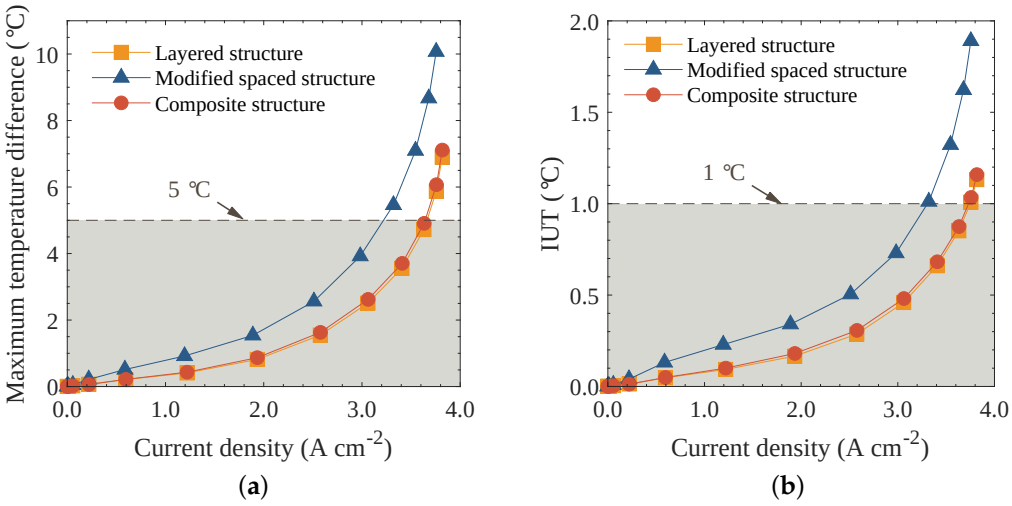

Figure 8. Impact of the HPBP internal structures on the temperature uniformity over the middle plane of the CCL: (**a**) Maximum temperature difference. (**b**) Index of uniform temperature.

Figure 9 demonstrates the polarization and power density curves for PEMFCs cooled by HPBPs with different internal structures. There is a slight difference between three cases in all current densities. The limiting current density corresponding to the layered, modified spaced, and composite structure of the HPBPs are 3.82 A cm^{-2}, 3.76 A cm^{-2}, and 3.82 A cm^{-2}, respectively. The three internal structures corresponds to a maximum power density of 1.53 W cm^{-2}, 1.49 W cm^{-2}, and 1.53 W cm^{-2}, respectively. It is worth mentioning that the current state-of-the-art fuel cell power density is 1.60 W cm^{-2}, which is obtained by The European Union Fuel Cells and Hydrogen 2 Joint Undertaking at a current density of 2.67 A cm^{-2} and a cell voltage of 0.6 V [43]. Therefore, the fuel cell studied in this paper belongs to the high power density fuel cell, and related discussions can guide the development of hydrogen energy UAM power system. The reason why the PEMFC cooled by modified spaced structural HPBP have worse cell performance is mainly due to its higher heat pipe thermal resistance. The thermal resistance of heat pipes is defined as the temperature difference between the evaporator and condenser average temperatures divided by the heat load. The thermal load at a cell voltage of 0.45 V is roughly equivalent for all three cases, as shown in Table 5, but the thermal resistance of the HPBP with the modified spaced structure is 4–5 times larger than that with the other two structures.

Table 5. Thermal resistance of heat pipes with different internal structures at a cell voltage of 0.45 V.

Parameters	Layered Structure	Modified Spaced Structure	Composite Structure
$\overline{T_{eva}}$ (°C)	82.749	89.240	82.551
$\overline{T_{con}}$ (°C)	76.123	67.336	76.653
Heat load (W)	1.089	0.901	1.095
Thermal resistance (°C/W)	6.084	24.311	5.386

Additionally, considering the operating range limits for PEMFCs mentioned above, the limiting current and maximum power density corresponding to the modified spaced structure will be decreased to 2.44 A cm^{-2} and 1.35 W cm^{-2}, respectively. These to the layered structure will be reduced to 2.09 A cm^{-2} and 1.22 W cm^{-2}, respectively. For the composite structure, these will be adjusted to 3.41 A cm^{-2} and 1.53 W cm^{-2}, respectively. When compared to the layered and modified spaced structures, the available maximum power density of the composite structure is increased by 25% and 13%, respectively, indicating that the internal structure of the heat pipe has a significant impact on the operating range of the fuel cell.

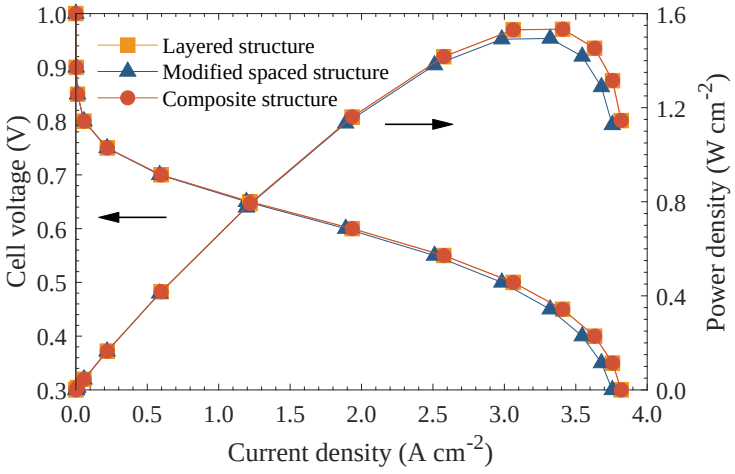

Figure 9. Comparison of the cell performance of PEMFCs cooled by HPBPs with different internal structures.

According to the results obtained, the composite structural HPBP outperforms the other two HPBPs in terms of thermal performance due to its low thermal resistance and reasonable arrangement of the limited internal cavity. Consequently, the composite structural HPBP cooled PEMFC is chosen as the research object to further reveal the influence of the LCWR on the local transport phenomena in the fuel cell.

3.2. Effect of the Lcwr on Heat and Mass Transport Phenomena in the Hpbp Cooled Pemfc

Dimensionless factors, such as the LCWR and the aspect ratio of the GCs, are crucial for optimizing system performance because of the features of HPBPs that couple the shape dimensions of the heat pipe and the bipolar plate. In view of the importance of the minimum shape dimensions of the vapor core, this study focuses exclusively on the LCWR. The detailed parameters in Table 6 are used to build cases with LCWRs of 0.75 and 1.33 in addition to the designs mentioned above. For all three designs, the sum of the land and channel widths is identical. The thermal resistance of HPBPs for these three LCWRs are 6.841 °C/W, 5.386 °C/W, and 4.688 °C/W, respectively. The PEMFC with a LCWR of 0.75 have a larger thermal resistance than that with a LCWR of 1.33 by 46%. The main cause of the difference in heat pipe thermal resistance is variation in vapor core size.

Table 6. Structural parameters and total thermal resistance of heat pipes for different LCWRs.

LCRW	0.75	1	1.33
Land width (mm)	0.6	0.7	0.8
Channel width (mm)	0.8	0.7	0.6
Cross-sectional dimensions of the vapore core (mm^2)	0.2 × 0.8	0.3 × 0.8	0.4 × 0.8
Thermal resistance of HPBPs @ 0.45 V (°C/W)	6.841	5.386	4.688

The operating range limits for PEMFCs with various LCWRs are shown in Figure 10. The maximum heat transfer capability of the HPBP for a LCWR of 0.75 is significantly lower than that for a LCWR of 1 or 1.33 due to the smaller size of the vapor core. The variation of the maximum temperature corresponding to the three LCWRs is almost the same at lower current densities. At high current densities, even though the LCWR of 1.33 corresponds to the lowest thermal resistance, the lowest efficiency leads to its highest maximum temperature.

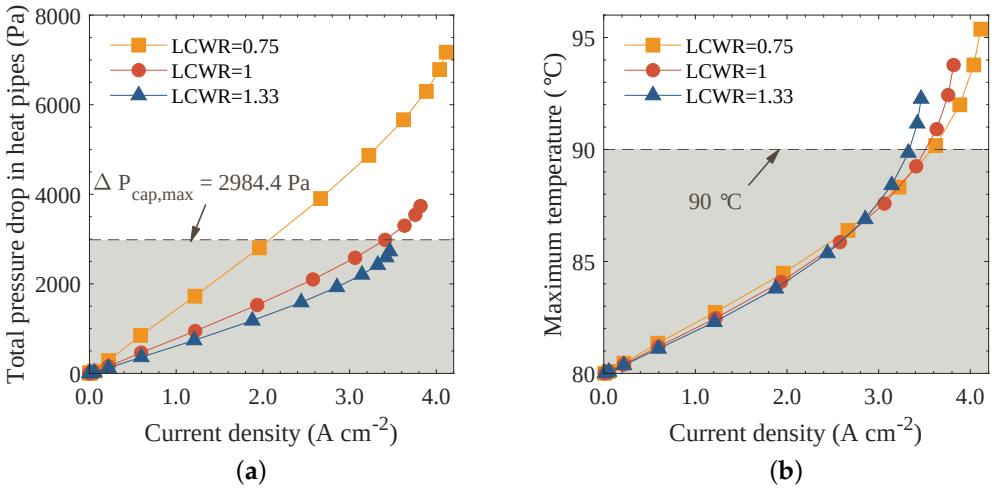

Figure 10. Comparison of the operating range limits for different LCWRs: (**a**) Maximum heat transfer capability. (**b**) Maximum temperature difference.

The polarization and power density curves for LCWRs of 0.75, 1, and 1.33 are shown in Figure 11. When the current density is less than 2.5 A cm^{-2}, the performances of the three LCWRs are nearly identical. With increasing current density, the LCWR of 0.75

outperforms the others, and the discrepancies in cell performance between different LCWRs are widening. The limiting current density for HPBP cooled PEMFC with LCWRs of 0.75, 1, and 1.33 is 4.11 A cm^{-2}, 3.82 A cm^{-2}, and 3.46 A cm^{-2}, respectively. Additionally, for these three designs, the maximum power density and corresponding cell voltage are 1.63 W cm^{-2} at 0.45 V, 1.53 W cm^{-2} at 0.45 V, and 1.43 W cm^{-2} at 0.50 V, respectively. The limiting current density and peak power density of the fuel cell with a LCWR of 0.75 are 19% and 14% higher than those with a LCWR of 1.33, respectively.

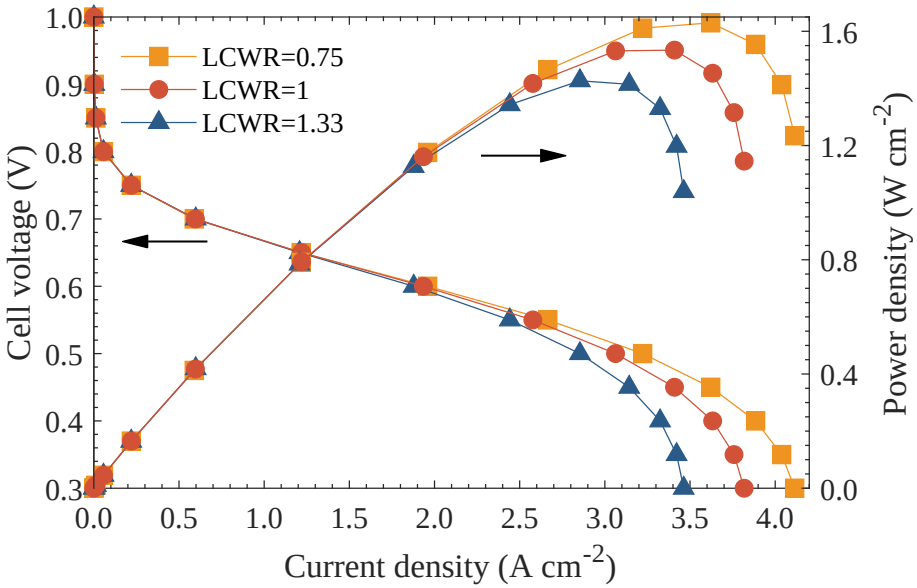

Figure 11. Comparison of the cell performance of PEMFCs cooled by HPBPs with different LCWRs.

The effect of LCWR variation on the heat and mass transport phenomena in PEMFC is the fundamental reason for the variance in electrochemical performance, in addition to the influence of heat pipe thermal resistance. The local distribution analysis is conducted for fuel cells in a cell voltage of 0.45 V. The temperature profile at the middle plane of the CCL for different LCWRs is displayed in Figure 12. The IUT for HPBP cooled PEMFC with LCWRs of 0.75, 1, and 1.33 is 0.62, 0.68, and 0.70, respectively, This suggests that smaller LCWRs have better temperature uniformity in the in-plane direction due to more evaporation. Higher temperatures are typically located towards the evaporator end of heat pipes, away from the condenser, but the figures demonstrate that the maximum temperatures are close to the condenser, with temperature increasing in the direction of air flow. This is due to the fact that the electrochemical reaction rate is limited by oxygen concentration at high current densities, resulting in more heat being generated in the cathode inlet. Figure 13 depicts the temperature distribution in the fuel cell's cross section at half length. It can be seen that the temperature of the PEMFC with a LCWR of 0.75 is higher than that of the fuel cells with LCWRs of 1 and 1.33 for the same cell voltage. The PEMFC with a LCWR of 1.33 provides the most uniform temperature distribution in the through-plane direction, and the PEMFC with a LCWR of 1 also outperforms that with a LCWR of 0.75. Because of the exponential character of the water vapor saturation curve, the temperature gradient in the through-plane direction would have a considerable effect on the two phase flow. Figure 13 also shows that temperature decreases in the direction from the channel to the land. The CCL has the highest temperature. Owing to the thin thinness of the MEA, the cathode temperature is only slightly higher than the anode temperature in this study.

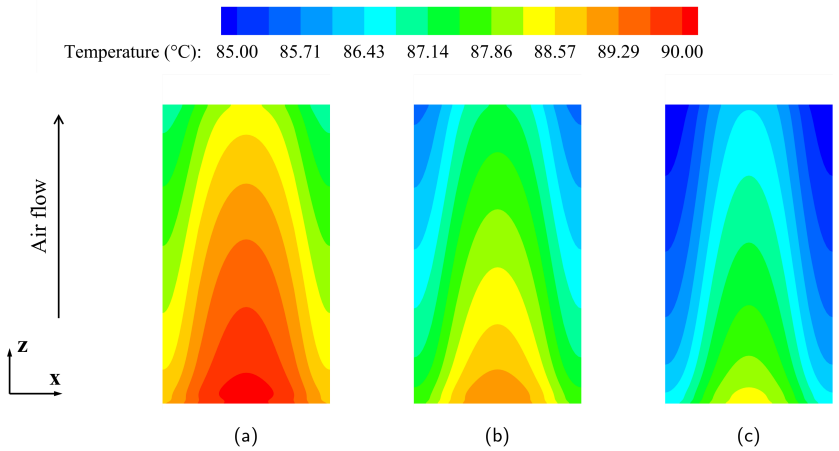

Figure 12. Impact of the LCWR on the temperature distribution over the middle plane of the CCL: (**a**) LCWR = 0.75. (**b**) LCWR = 1. (**c**) LCWR = 1.33.

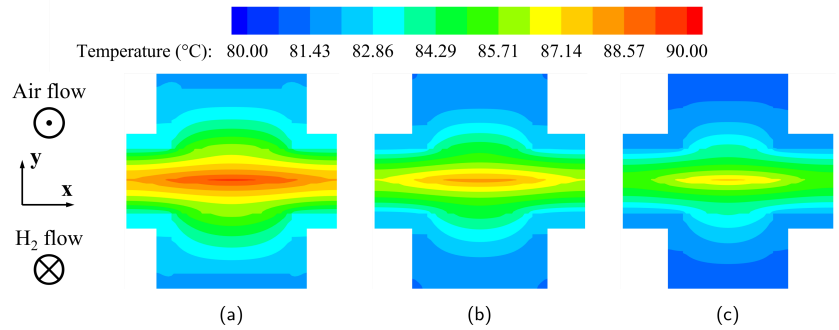

Figure 13. Impact of the LCWR on the temperature distribution over the middle plane of the PEMFCs in the z direction: (**a**) LCWR = 0.75. (**b**) LCWR = 1. (**c**) LCWR = 1.33.

Heat transfer is fundamentally coupled with water transport and phase change in PEMFCs. Figures 14 and 15 illustrate the distribution of liquid water saturation over ther middle plane of the CCL and the ACL, respectively. In the directions of reactant gas flow, liquid water accumulates at both the cathode and the anode. Because of the mass transfer resistance, liquid water tends to concentrate under the land; the larger the LCWR, the greater the liquid water mass transfer resistance and the more uneven distribution in the x-direction. Too much liquid water could obstruct reactant transport from GCs to active sites, increasing transport resistance and concentration polarization. According to the Figure 14, the maximum liquid water saturation for LCWRs of 0.75, 1, and 1.33 are 0.131, 0.137, and 0.141. The maximum value of liquid water saturation moves away from the cathode outlet as LCWR increases. The location of the maximum value of liquid water saturation moves away from the cathode outlet as LCWR rises. In the contours of these three cases, the regions with liquid water saturation greater than 0.13 account for 16%, 38%, and 79% of the total area. This suggests that an increase in LCWR leads to a rapid increase in the area proportion of high liquid water saturation, making the fuel cell more prone to flooding. As illustrated in Figure 15, the liquid water distribution on the ACL side is more linear compared to the CCL side due to the sufficient hydrogen supply. The ACL contains more liquid water than the CCL due to the low temperature leading more water vapor to condense. It is worth mentioning that a smaller LCWR corresponds to a higher peak value of liquid water saturation at the ACL side, which is contrary to the situation on the CCL side.

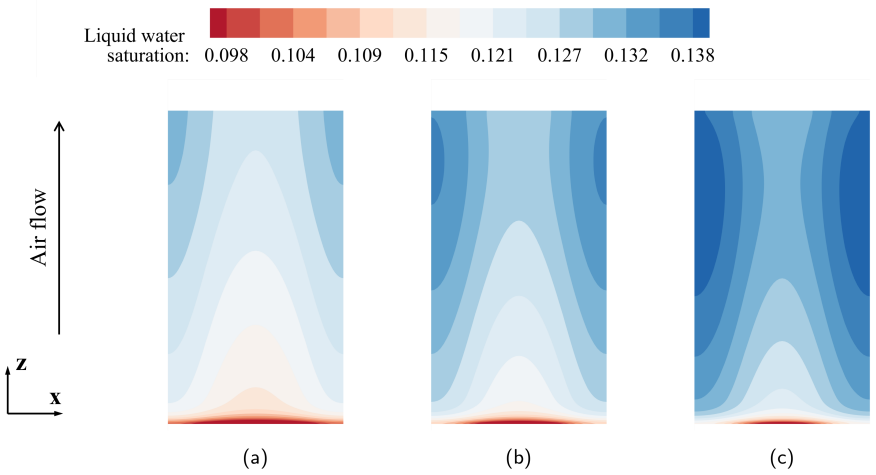

Figure 14. Impact of the LCWR on the liquid water saturation over the middle plane of the CCL: (**a**) LCWR = 0.75. (**b**) LCWR = 1. (**c**) LCWR = 1.33.

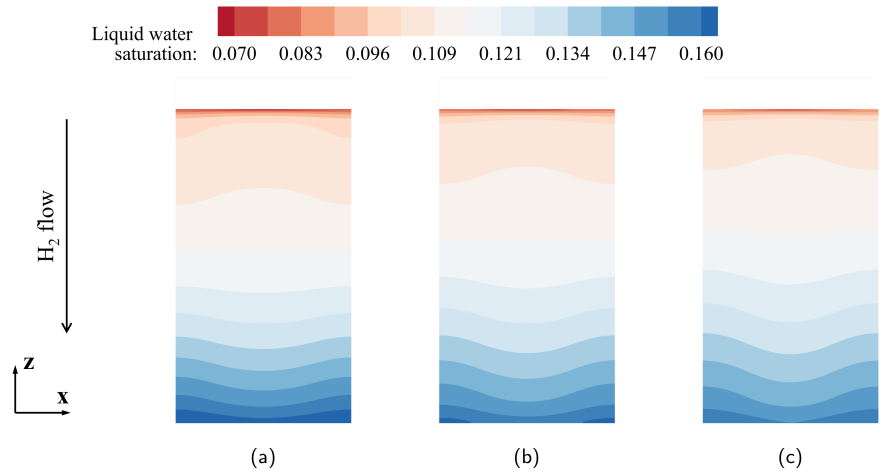

Figure 15. Impact of the LCWR on the liquid water saturation over the middle plane of the ACL: (**a**) LCWR = 0.75. (**b**) LCWR = 1. (**c**) LCWR = 1.33.

Figure 16 demonstrates the comparison of the current density over the middle plane of the MEM for different LCWRs, in which the smaller the LCWR the more high current density regions in the x-direction. Due to the hight inlet relative humidity of 95%, the membrane drying-out phenomenon will not occur, impling that the oxygen distribution governs the current density profile along the flow direction. As shown in Figure 17, it is evident that as the oxygen concentration declines, the current density roughly decreases along the air flow. The trends of the current density in the x-direction is also closely related to that of oxygen concentration. Due to the fact that the concentration loss is the main performance limitation at high current densities, the region under the channel usually exhibits a significantly higher current density. For the operating voltage of 0.45 V, the minimum molar concentration of oxygen at the middle plane of the CLL is about 0.05 mol m^{-3}, suggesting a severe oxygen deficiency.

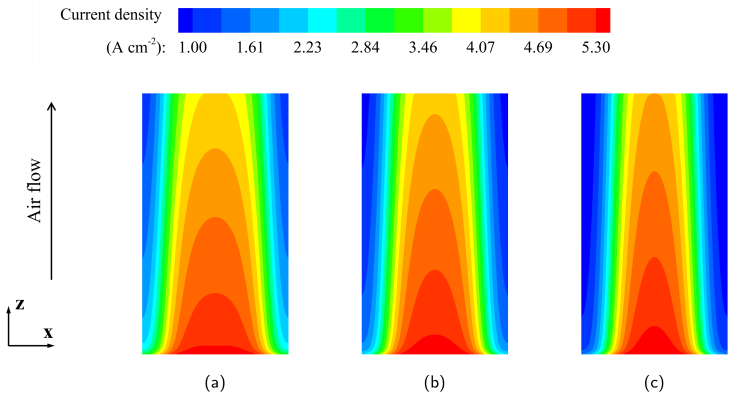

Figure 16. Impact of the LCWR on the current density over the middle plane of the MEM: (**a**) LCWR = 0.75. (**b**) LCWR = 1. (**c**) LCWR = 1.33.

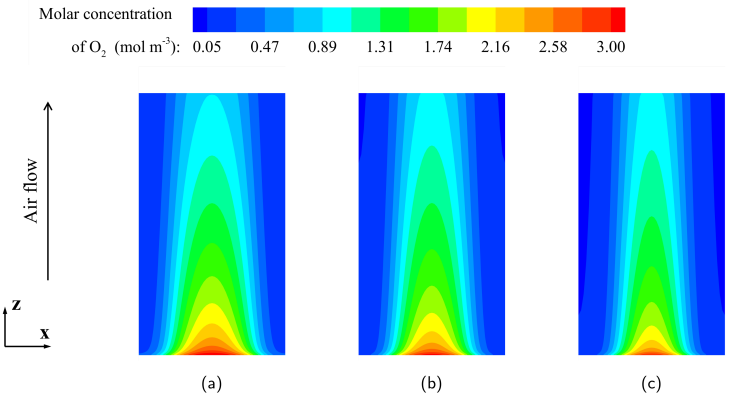

Figure 17. Impact of the LCWR on the oxygen concentration over the middle plane of the CCL: (**a**) LCWR = 0.75. (**b**) LCWR = 1. (**c**) LCWR = 1.33.

4. Conclusions

The fundamental limitation of fuel cell devices for urban air mobility applications is their poor power density. Heat pipe cooled fuel cells have the potential to considerably enhance fuel cell power density, but the impact of heat pipe internal structure on fuel cell power density and operating range is very limited. In this study, representative internal structures are designed for the heat pipe bipolar plate cooling, including layered, modified spacing, and composite structures. A three-dimensional multiphase non-isothermal single channel model is developed to investigate the thermal and electrochemical performance of the heat pipe bipolar plate cooled PEMFC. The effect of the internal structure of the heat pipe on the thermal performance of the heat pipe cooled PEMFC is elucidated. The operating range of the fuel cell constrained by the maximum heat transfer capability, maximum temperature, and temperature uniformity is analyzed and discussed. Furthermore, the relation between land to channel width ratio and local heat and mass transport phenomena is investigated. The following essential conclusions can be derived:

- The polarization curves of PEMFCs cooled by heat pipes with different internal structures show little difference, but the operating range varies significantly. Since it has a low thermal resistance and appropriate arrangement of the limited internal cavity, the PEMFC cooled by the composite structural heat pipe bipolar plate has a limiting current and maximum power density that are 63% and 25% higher than those cooled by the layered structural heat pipe bipolar plate and 40% and 13% higher than those cooled by the modified spaced structural heat pipe bipolar plate, respectively.
- The heat pipe bipolar plate cooled PEMFC with a land to channel width ratio of 0.75 has a significant advantage in cell performance at high current densities compared to the land to channel width ratios of 1 and 1.33. The limiting current density and

maximum power density of the heat pipe bipolar plate cooled PEMFC with a land to channel width ratioof 0.75 are 19% and 14% higher than those with a land to channel width ratio of 1.33, respectively.

- For temperature distribution, the lower the land to channel width ratio, the better the in-plane uniformity and the worse the through-plane uniformity. Reducing the land to channel width ratio improves liquid water distribution uniformity on the cathode side while having the reverse effect on the anode side.

Author Contributions: Y.H. and W.Z. proposed innovative points on the analysis of the thermal and electrochemical performace of the heat pipe cooled PEMFCs with various internal structures. Y.H. performed the calculations and paper writing. Y.H., J.P. and Y.Q. performed the investigation and validation. W.Z. and Y.Z. performed the review and editing of the paper. All authors have read and agreed to the published version of the manuscript.

Funding: This study was financially supported by the National Natural Science Foundation of China (No. U1864212).

Institutional Review Board Statement: Not applicable.

Informed Consent Statement: Not applicable.

Data Availability Statement: Not applicable.

Conflicts of Interest: The authors declare no conflict of interest.

Nomenclature

m	Mass flow rates, kg s^{-1}
V	Voltage, V
T	Temperature, K
P	Pressure, Pa
s	Liquid water saturation
H	Henry's coefficient, Pa m^3 mol^{-1}
i	Exchange current density, A m^{-2}
A	Effective surface area, m^{-1}
a	Water activity
K	Permeability, m^{-2}
D	Diffusivity, m^2 s^{-1}
S	Source terms
Y	Mass fraction
$\boldsymbol{u}$	Superficial velocity, m s^{-1}
c_p	Specific heat capacity, J kg^{-1} K^{-1}
k	Thermal conductivity, W m^{-1} K^{-1}
L	Latent heat, J kg^{-1}
R	Universal gas constant, 8.314 J K^{-1} mol^{-1}
F	Faraday's constant, 96,487 C mol^{-1}
j	Volumetric current density, A m^{-3}
C	Gas molar concentration, mol m^{-3}
Greek letters	
δ	Thickness, m
α	Transfer coefficient
η	Overpotential, V
ϕ	Potential, V
λ	Membrane water content
μ	Dynamic viscosity, kg m^{-1} s^{-1}
ρ	Density, kg m^{-3}
σ	Surface tension coefficient, N m^{-1}
θ	Contact angle, $^\circ$
ε	Porosity/Volume fraction
ω	Ionomer volume fraction

$\kappa_e, \kappa_!$	Electric and protonic conductivity, S m^{-1}
γ_a, γ_d	Adsorption and desorption rates of dissolved water, s^{-1}
$\zeta_{cond}, \zeta_{evap}$	Condensation and evaporation rates of water, s^{-1}
Subscripts and superscripts	
eff	Effective
ref	Reference state
l	Liquid water
v	water vapor
a	Anode
c	Cathode
act	Activation state
sat	Saturation state
eq	Equilibrium
cap	Capillary
i	Gas species
agg	Agglomerate
ω	Ionomer
Abbreviations	
PEMFC	proton exchange membrane fuel cell
eVTOL	electric vertical takeoff and landing
HPBP	heat pipe bipolar plate
UAM	urban air mobility
LCWR	land to channel width ratio
MEM	polymer exchange membrane
CBP/ABP	cathode/anode bipolar plate
CGC/AGC	cathode/anode gas channel
CGDL/AGDL	cathode/anode gas diffusion layer
CCL/ACL	cathode/anode catalyst layer

References

1. Garrow, L.A.; German, B.J.; Leonard, C.E. Urban air mobility: A comprehensive review and comparative analysis with autonomous and electric ground transportation for informing future research. *Transp. Res. Part Emerg. Technol.* **2021**, *132*, 103377. [CrossRef]
2. Bauranov, A.; Rakas, J. Designing airspace for urban air mobility: A review of concepts and approaches. *Prog. Aerosp. Sci.* **2021**, *125*, 100726. [CrossRef]
3. Ahluwalia, R.K.; Peng, J.K.; Wang, X.; Papadias, D.; Kopasz, J. Performance and cost of fuel cells for urban air mobility. *Int. J. Hydrogen Energy* **2021**, *46*, 36917–36929. [CrossRef]
4. Liu, T.; Yang, X.G.; Ge, S.; Leng, Y.; Wang, C.Y. Ultrafast charging of energy-dense lithium-ion batteries for urban air mobility. *eTransportation* **2021**, *7*, 100103. [CrossRef]
5. Lei, T.; Min, Z.; Gao, Q.; Song, L.; Zhang, X.; Zhang, X. The Architecture Optimization and Energy Management Technology of Aircraft Power Systems: A Review and Future Trends. *Energies* **2022**, *15*, 4109. [CrossRef]
6. Zhao, R.; Qin, D.; Chen, B.; Wang, T.; Wu, H. Thermal Management of Fuel Cells Based on Diploid Genetic Algorithm and Fuzzy PID. *Appl. Sci.* **2023**, *13*, 520. [CrossRef]
7. Ng, W.; Datta, A. Hydrogen Fuel Cells and Batteries for Electric-Vertical Takeoff and Landing Aircraft. *J. Aircr.* **2019**, *56*, 1765–1782. [CrossRef]
8. Chakraborty, S.; Elangovan, D.; Palaniswamy, K.; Fly, A.; Ravi, D.; Seelan, D.A.S.; Rajagopal, T.K.R. A Review on the Numerical Studies on the Performance of Proton Exchange Membrane Fuel Cell (PEMFC) Flow Channel Designs for Automotive Applications. *Energies* **2022**, *15*, 520. [CrossRef]
9. Pan, Z.F.; An, L.; Wen, C.Y. Recent advances in fuel cells based propulsion systems for unmanned aerial vehicles. *Appl. Energy* **2019**, *240*, 473–485. [CrossRef]
10. Huang, Y.; Xiao, X.; Kang, H.; Lv, J.; Zeng, R.; Shen, J. Thermal management of polymer electrolyte membrane fuel cells: A critical review of heat transfer mechanisms, cooling approaches, and advanced cooling techniques analysis. *Energy Convers. Manag.* **2022**, *254*, 5221. [CrossRef]
11. Xiong, S.; Wu, Z.; Li, W.; Li, D.; Zhang, T.; Lan, Y.; Zhang, X.; Ye, S.; Peng, S.; Han, Z.; et al. Improvement of Temperature and Humidity Control of Proton Exchange Membrane Fuel Cells. *Sustainability* **2021**, *13*, 578. [CrossRef]
12. Li, Q.; Liu, Z.; Sun, Y.; Yang, S.; Deng, C. A Review on Temperature Control of Proton Exchange Membrane Fuel Cells. *Processes* **2021**, *9*, 235. [CrossRef]

13. Silva, A.P.; Galante, R.M.; Pelizza, P.R.; Bazzo, E. A combined capillary cooling system for fuel cells. *Appl. Therm. Eng.* **2012**, *41*, 104–110. [CrossRef]
14. Clement, J.; Wang, X. Experimental investigation of pulsating heat pipe performance with regard to fuel cell cooling application. *Appl. Therm. Eng.* **2013**, *50*, 268–274. [CrossRef]
15. Shirzadi, N.; Roshandel, R.; Shafii, M.B. Integration of Miniature Heat Pipes into a Proton Exchange Membrane Fuel Cell for Cooling Applications. *Heat Transf. Eng.* **2016**, *38*, 1595–1605. [CrossRef]
16. Min, C.; Gao, X.; Li, F.; Wang, K. Thermal performance analyses of pulsating heat pipe for application in proton exchange member fuel cell. *Energy Convers. Manag.* **2022**, *259*, 5566. [CrossRef]
17. Faghri, A. Integrated Bipolar Plate Heat Pipe for Fuel Cell Stacks. U.S. Patent Application No. 10/640, 17 February 2005.
18. Oro, M.V.; Bazzo, E. Flat heat pipes for potential application in fuel cell cooling. *Appl. Therm. Eng.* **2015**, *90*, 848–857. [CrossRef]
19. Bulut, M.; Kandlikar, S.G.; Sozbir, N. A Review of Vapor Chambers. *Heat Transf. Eng.* **2018**, *40*, 1551–1573. [CrossRef]
20. Huang, B.; Jian, Q.; Luo, L.; Bai, X. Research on the in-plane temperature distribution in a PEMFC stack integrated with flat-plate heat pipe under different startup strategies and inclination angles. *Appl. Therm. Eng.* **2020**, *179*, 115741. [CrossRef]
21. Wang, L.; Quan, Z.; Zhao, Y.; Yang, M.; Zhang, J. Experimental investigation on thermal management of proton exchange membrane fuel cell stack using micro heat pipe array. *Appl. Therm. Eng.* **2022**, *214*, 8831. [CrossRef]
22. Zhao, J.; Huang, Z.; Jian, B.; Bai, X.; Jian, Q. Thermal performance enhancement of air-cooled proton exchange membrane fuel cells by vapor chambers. *Energy Convers. Manag.* **2020**, *213*, 112830. [CrossRef]
23. Lv, L.; Li, J. Managing high heat flux up to 500 W/cm^2 through an ultra-thin flat heat pipe with superhydrophilic wick. *Appl. Therm. Eng.* **2017**, *122*, 593–600. [CrossRef]
24. Tang, H.; Tang, Y.; Wan, Z.; Li, J.; Yuan, W.; Lu, L.; Li, Y.; Tang, K. Review of applications and developments of ultra-thin micro heat pipes for electronic cooling. *Appl. Energy* **2018**, *223*, 383–400. [CrossRef]
25. Tang, Y.; Hong, S.; Wang, S.; Deng, D. Experimental study on thermal performances of ultra-thin flattened heat pipes. *Int. J. Heat Mass Transf.* **2019**, *134*, 884–894. [CrossRef]
26. Zhou, W.; Li, Y.; Chen, Z.; Deng, L.; Gan, Y. A novel ultra-thin flattened heat pipe with biporous spiral woven mesh wick for cooling electronic devices. *Energy Convers. Manag.* **2019**, *180*, 769–783. [CrossRef]
27. Zhou, W.; Xie, P.; Li, Y.; Yan, Y.; Li, B. Thermal performance of ultra-thin flattened heat pipes. *Appl. Therm. Eng.* **2017**, *117*, 773–781. [CrossRef]
28. Li, Y.; Zhou, W.; He, J.; Yan, Y.; Li, B.; Zeng, Z. Thermal performance of ultra-thin flattened heat pipes with composite wick structure. *Appl. Therm. Eng.* **2016**, *102*, 487–499. [CrossRef]
29. Huang, G.; Liu, W.; Luo, Y.; Deng, T.; Li, Y.; Chen, H. Research and optimization design of limited internal cavity of ultra-thin vapor chamber. *Int. J. Heat Mass Transf.* **2020**, *148*, 119101. [CrossRef]
30. Zhou, W.; Li, Y.; Chen, Z.; Deng, L.; Gan, Y. Effect of the passage area ratio of liquid to vapor on an ultra-thin flattened heat pipe. *Appl. Therm. Eng.* **2019**, *162*, 4215. [CrossRef]
31. Huang, G.; Liu, W.; Luo, Y.; Li, Y. A novel ultra-thin vapor chamber for heat dissipation in ultra-thin portable electronic devices. *Appl. Therm. Eng.* **2020**, *167*, 4726. [CrossRef]
32. Guangwen, H.; Wangyu, L.; Yuanqiang, L.; Yong, L.; Hanyin, C. Fabrication and capillary performance of a novel composite wick for ultra-thin heat pipes. *Int. J. Heat Mass Transf.* **2021**, *176*, 1467. [CrossRef]
33. Ma, X.; Zhang, X.; Yang, J.; Zhuge, W.; Shuai, S. Impact of gas diffusion layer spatial variation properties on water management and performance of PEM fuel cells. *Energy Convers. Manag.* **2021**, *227*. [CrossRef]
34. Chen, H.; Guo, H.; Ye, F.; Ma, C.F. Modification of the two-fluid model and experimental study of proton exchange membrane fuel cells with baffled flow channels. *Energy Convers. Manag.* **2019**, *195*, 972–988. [CrossRef]
35. Zhang, G.; Jiao, K. Three-dimensional multi-phase simulation of PEMFC at high current density utilizing Eulerian-Eulerian model and two-fluid model. *Energy Convers. Manag.* **2018**, *176*, 409–421. [CrossRef]
36. Zhang, G.; Wu, J.; Wang, Y.; Yin, Y.; Jiao, K. Investigation of current density spatial distribution in PEM fuel cells using a comprehensively validated multi-phase non-isothermal model. *Int. J. Heat Mass Transf.* **2020**, *150*, 9294. [CrossRef]
37. Xing, L.; Liu, X.; Alaje, T.; Kumar, R.; Mamlouk, M.; Scott, K. A two-phase flow and non-isothermal agglomerate model for a proton exchange membrane (PEM) fuel cell. *Energy* **2014**, *73*, 618–634. [CrossRef]
38. Xu, Y.; Fan, R.; Chang, G.; Xu, S.; Cai, T. Investigating temperature-driven water transport in cathode gas diffusion media of PEMFC with a non-isothermal, two-phase model. *Energy Convers. Manag.* **2021**, *248*, 114791. [CrossRef]
39. Moein-Jahromi, M.; Kermani, M.J. Three-dimensional multiphase simulation and multi-objective optimization of PEM fuel cells degradation under automotive cyclic loads. *Energy Convers. Manag.* **2021**, *231*, 3837. [CrossRef]
40. Brahim, T.; Jemni, A. CFD analysis of hotspots copper metal foam flat heat pipe for electronic cooling applications. *Int. J. Therm. Sci.* **2021**, *159*, 106583. [CrossRef]
41. Koito, Y. Numerical analyses on heat transfer characteristics of ultra-thin heat pipes: Fundamental studies with a three-dimensional thermal-fluid model. *Appl. Therm. Eng.* **2019**, *148*, 430–437. [CrossRef]

42. Ren, P.; Pei, P.; Chen, D.; Li, Y.; Wang, H.; Fu, X.; Zhang, L.; Wang, M.; Song, X. Micro-current excitation for efficient diagnosis of membrane electrode assemblies in fuel cell stacks: Error analysis and method optimization. *Energy Convers. Manag.* **2022**, *258*, 115489. [CrossRef]
43. Jiao, K.; Xuan, J.; Du, Q.; Bao, Z.; Xie, B.; Wang, B.; Zhao, Y.; Fan, L.; Wang, H.; Hou, Z.; et al. Designing the next generation of proton-exchange membrane fuel cells. *Nature* **2021**, *595*, 361–369. [CrossRef] [PubMed]